Shock-Wave/Boundary-Layer Interactions at Compression Ramps Studied by High-Speed Schlieren

Zhengzhong Sun[1]

City, University of London, London, UK, EC1V 0HB

Tian Gan[2], Yun Wu [3]

Xi'an Jiaotong University, Xi'an, China, 710076

Abstract

The shock wave boundary layer interactions (SWBLIs) at compression ramps (ramp angle α=20°-30°) are studied at Ma=2.0 and under two Reynolds numbers (Re_1=18,600 and Re_2=35,600, *Re* based on boundary layer thickness). High-speed schlieren operating at 20 kHz is used as the flow diagnostics. The flow structures in the compression ramp SWBLIs, including the shock wave, interaction region and induced turbulent region over the ramp surface, are discussed. Their variation under increasing ramp angle and Reynolds number are further examined. The low-frequency shock wave oscillations are also studied through tracking the shock wave motion. A larger ramp angle increases the spectral intensity of the shock wave's low-frequency unsteadiness, while increasing the Reynolds number results in a lower peak frequency for the separation and reattachment shock waves.

Nomenclature

f	=	frequency
h	=	ramp height
I	=	schlieren intensity
l	=	the length of model top surface upstream of the ramp

[1] Senior Lecturer, Department of Mechanical Engineering and Aeronautics, Northampton Square
[2] Lecturer, Department of Mechanical Engineering, 28 Xianning West Road
[3] Professor, Department of Mechanical Engineering, 28 Xianning West Road

L = length of interaction region

Ma = Mach number

N = number of images

P = spectrum magnitude

Re = Reynolds number

St = Strouhal number

U_∞ = free stream velocity

x = the streamwise coordinate

y = the wall-normal coordinate

α = ramp angle

δ = boundary layer thickness

ε = residual

Subscript

i = interaction

L = length of interaction region

$mean$ = mean flow quantity

RMS = root-mean-square

s = separation

$1,2$ = Reynolds number 1 and 2

θ = boundary layer momentum thickness

I. Introduction

The shock wave boundary layer interaction (SWBLI) is a critical phenomenon in transonic and supersonic aerodynamics. The occurrence of a SWBLI gives rise to unsteady flow separation and enhanced turbulence intensity, which induces drag and affects aerodynamic efficiency. As the SWBLI underpins many transonic and supersonic applications, a lot of research efforts have been attracted for more than half a century [1]. The SWBLIs at the compression ramp [2] and those induced by an oblique incident oblique shock wave [3] are widely adopted as the

baseline cases, and in-depth fundamental understandings have been generated. These two types of SWBLI also represent simplified geometries encountered in practical aerodynamic applications, such as the supersonic inlet [4,5]. The present research chooses to examine the SWBLI established at a compression ramp.

The compression ramp induced SWBLI has been studied through experimental and numerical methods under different Mach numbers and Reynolds numbers. A comprehensive summary is provided in the monograph dedicated to SWBLI [6]. Knowledge on the overall flow structure has been well established. The major flow features include the separation and reattachment shock waves, the interaction region, and the boundary layer separation and re-attachment. The length of the interaction region is one important parameter. Its growth with increasing ramp angle has been studied through a series of experiments at Ma=3.0 by Zheltovodov [7]. This research was thereafter used as the benchmark case for simulation validation [2,8,9]. In the DNS study of a 24° compression ramp at Ma=2.9 [2], the leading edge of the time-averaged interaction region extended to $x_s/\delta = -2.1$, where the origin of the x-axis was at the ramp foot. Another LES simulation on a 25° compression ramp at Ma = 2.88 revealed that the interaction started from $x_s/\delta = -4.0$ [8], which is nearly doubled from that in [2]. The different interaction length is likely a result of the Reynolds number effect, as the two SWBLIs were simulated under Re_θ = 2,900 and 5,385, respectively. Therefore, a larger Reynolds number produces a longer non-dimensional interaction region. A more recent DNS study on a 25° ramp at Ma = 2.9 and Re_θ = 2,372 revealed a separation length of $x_s/\delta = -2.44$ [9], which confirmed the Reynolds number effect, as it is close to that in [7]. Reviewing the literature on supersonic compression ramps, most of the works have Mach numbers around 3.0. In contrast, researches on a lower Mach number, such as Ma=2.0, are less systematic. Moreover, a lower Mach number around 2.0 is also relevant to the commercial supersonic transportation that is currently being re-investigated. Hence, the present experiment aims to analyse SWBLIs at compression ramps under Ma=2.0 flow. At the same time, the Reynolds number effect will also be examined.

The interaction region features low-frequency unsteadiness in SWBLI, which is two magnitudes smaller than that in the incoming turbulent boundary layer [10]. Researches have been directed to explore the origin of the low-frequency unsteadiness, so that an appropriate flow control method can be designed. The upstream and downstream sources of the low-frequency unsteadiness have been identified and summarized in a review article [11]. The surface pressure sampled at a fast recording rate is utilized to reveal the unsteadiness in SWBLI. In the work of Dupont et al. [10] on an incident shock SWBLI, the low-frequency shock oscillation had St_L = 0.02−0.05, where St_L is the Strouhal number based on interaction length. Priebe & Martin [2] found that the power spectrum of the fluctuating pressure

inside the interaction region was broadband in general. In particular, the spectrum at the shock wave location has an intensified energy in the band of $\boldsymbol{St_\delta}$ = 0.002−0.03 (peak magnitude at $\boldsymbol{St_\delta}$ = 0.01), while the pressure power spectra within the interaction region exhibit enhanced energy in a higher band of $\boldsymbol{St_\delta}$ = 0.04−5. Grilli et al. [12] reported an even lower peak frequency for the shock oscillation, namely St_δ = 0.004, whereas the wall pressure power spectra at locations inside the separation region shifted towards higher *St* numbers, which were still smaller than those in the incoming boundary layer. Another objective of the present study is to reveal the shock wave unsteadiness, especially the modulation of shock wave spectrum under the influence of the ramp angle and Reynolds number. Instead of measuring the instantaneous wall pressure, the temporal motion of the shock wave is tracked through schlieren images recorded at high-sampling rate, namely the schlieren is used as an optical sensor.

In summary, the present experimental research on compression ramp SWBLIs is conducted to study the Reynolds number effect on the SWBLI structure, as well as the shock wave unsteadiness. Six ramps with angles ranging from 20° to 30° with an interval of 2° are measured, so that the effect of ramp angle, or interaction strength, can also be revealed. High-speed schlieren operating at 20 kHz is used as the flow instrumentation. In the remainder of the paper, the experimental setup is first introduced, followed by the detailed discussions on the experimental results reflecting the ramp angle effect and Reynolds number effect. Conclusions are finally drawn at the end of the paper.

II. Experimental Setup

A. Wind Tunnel and Test Models

The supersonic wind tunnel at Xi'an Jiaotong University is used as the flow facility. This wind tunnel is a suction type facility. The flow is driven by the pressure difference between the ambient and the vacuum downstream of the diffuser. The total pressure and total temperature are 1 atm and 300 K, respectively. In the experiment, a Mach 2.0 nozzle is used. Before the nozzle inlet, a cluster of 18 fine mesh screens is used to straighten the flow and reduce turbulence. The nozzle outlet has a diameter of 300 mm, and the supersonic free jet enters a cylindrical test chamber with a diameter of 1.5 m, which is made big enough to eliminate wall interference towards the supersonic flow. The test chamber connects to a 120 m^3 vacuum tank through a diffuser.

The Perspex test model is comprised of two parts, the base plate with flat top surface and the ramp piece. Two base plates with different length are available. The longer plate allows further development of the turbulent boundary layer, resulting in a larger boundary layer thickness. Both plates have the same width of w = 110 mm. Six

ramp pieces are going to be tested, their angles are α = 20°–30° with an interval of 2°. All the ramp pieces have the same height of h = 20 mm and are topped by a flat surface. The ramp is installed l_1 = 150 mm from the leading edge on the shorter plate, while l_2 = 360 mm on the longer plate. The compression ramp model is sketched in figure 1(a). The boundary layer at the location of the ramp is found to have a thickness of 2.3 mm and 4.4 mm for the two models respectively through schlieren visualization. A separate PIV measurement revealed that the free stream velocity is 514 m/s and the turbulence intensity is about 1%. The Reynolds number based on boundary layer thickness is Re_1 = 18,600 and Re_2 = 35,600, respectively. The model is installed onto the mounting plate at the bottom of the test chamber through a wedge-shaped vertical strut. The installation of the test model is sketched conceptually in figure 1(b). The relevant flow and model parameters are summarized in Table 1.

Table 1. Flow and model parameters

Parameter	**Quantity**	
Mach number	$\boldsymbol{Ma}$ = 2.0	
Free stream velocity	$\boldsymbol{U_\infty}$ = 514±5 m/s	
Ramp height	$\boldsymbol{h}$ = 20 mm	
Ramp angle	$\boldsymbol{\alpha}$ = 20°, 22°, 24°, 26°, 28°, 30°	
Streamwise length for boundary layer development	$\boldsymbol{l_1}$ =150 mm	$\boldsymbol{l_2}$ = 360 mm
Boundary layer thickness	$\boldsymbol{\delta_1}$ = 2.3 mm	$\boldsymbol{\delta_2}$ =4.4 mm
Reynolds number (based on $\boldsymbol{\delta}$)	$\boldsymbol{Re_1}$ =18,600	$\boldsymbol{Re_2}$ =35,600

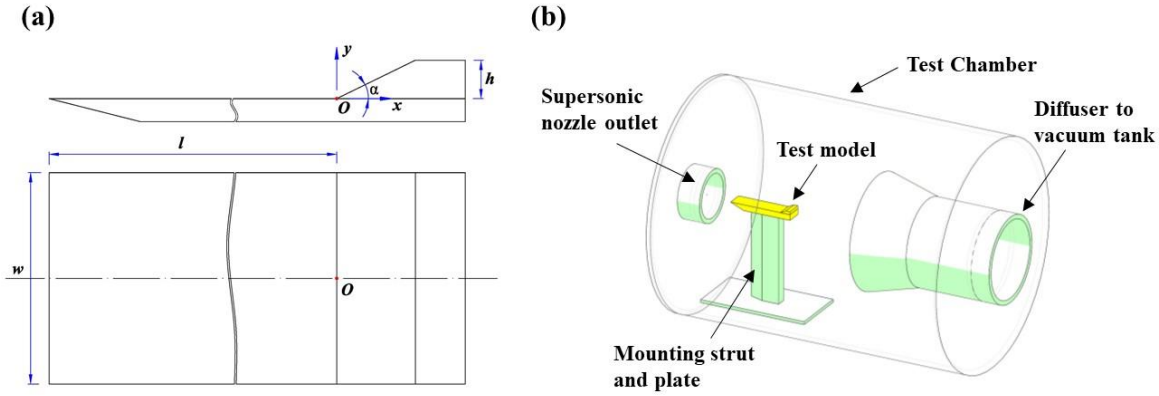

Fig. 1 The compression ramp model with coordinate system (a) and its installation in the wind tunnel (b).

B. High-Speed Schlieren

The present schlieren setup follows a *Z*-type light path. The illumination is provided by a Gloria 500W Xenon lamp. A Phantom V2512 ultra-high-speed camera is used to record the schlieren images. The camera sensor has 1280×800 pixels with 20 μm pixel pitch. The field of view covers an area of 237×148 mm^2, resulting in a spatial resolution of 0.185 mm/pixel and a magnification factor of 0.11. The acquisition is initiated as soon as the wind tunnel flow starts. The knife-edge is placed vertically, hence the horizontal density gradient is amplified. The schlieren setup remains the same for both Reynolds number cases. The image acquisition frequency is 20 kHz, so that the temporal motion of the shock wave can be resolved. The camera exposure time is set to 1 μs to freeze the turbulent structures.

Schlieren is mostly used as a qualitative flow visualization technique for the shock wave and other flow structures where a large density gradient is present. With some fine tunings of the schlieren setup, such as reducing the camera exposure time or using nanosecond pulsed light source (e.g. the spark light and pulsed laser), the flow structures can be captured with sharp edges. For example, a recent schlieren experiment using a pulsed laser successfully visualized the intermittent vortical structure in hypersonic boundary layer transition [13].

Apart from qualitative observation of the schlieren snapshots, the RMS schlieren intensity field was used as a semi-quantitative way to reveal the flow field fluctuations. A recent experimental study by Combs et al. [14] on transitional SWBLI visualized the amplification of fluctuation intensity in the separation region of transitional SWBLIs under increasing Reynolds numbers. The statistics of the recorded schlieren intensity fields, namely the mean (I_{mean}) and the root-mean-square (I_{RMS}), are also examined in this paper. The convergence of the two statistical quantities are enabled by the large image ensemble. For the SWBLIs at Re_1, the dataset for each ramp case has 10,000 images, while 9,000 images for each case at Re_2. A residual quantity ε is defined, which is the maximum absolute difference between $\boldsymbol{I}(\boldsymbol{i},\boldsymbol{j})_{mean}^{\boldsymbol{N}}$ and $\boldsymbol{I}(\boldsymbol{i},\boldsymbol{j})_{mean}^{\boldsymbol{N-1}}$ or between $\boldsymbol{I}(\boldsymbol{i},\boldsymbol{j})_{RMS}^{\boldsymbol{N}}$ and $\boldsymbol{I}(\boldsymbol{i},\boldsymbol{j})_{RMS}^{\boldsymbol{N-1}}$, namely

$$\varepsilon_{I_{mean}} = \max(|\boldsymbol{I}(\boldsymbol{i},\boldsymbol{j})_{mean}^{\boldsymbol{N}} - \boldsymbol{I}(\boldsymbol{i},\boldsymbol{j})_{mean}^{\boldsymbol{N-1}}|)$$

$$\varepsilon_{I_{RMS}} = \max(|\boldsymbol{I}(\boldsymbol{i},\boldsymbol{j})_{rms}^{\boldsymbol{N}} - \boldsymbol{I}(\boldsymbol{i},\boldsymbol{j})_{rms}^{\boldsymbol{N-1}}|)$$

where $\boldsymbol{I}(\boldsymbol{i},\boldsymbol{j})_{mean}^{\boldsymbol{N}}$ is the mean schlieren intensity field based on a number of *N* images, and $(\boldsymbol{i},\boldsymbol{j})$ is the $\boldsymbol{i}^{\boldsymbol{th}}$ and $\boldsymbol{j}^{\boldsymbol{th}}$ pixel along the horizonal and vertical direction, respectively. The evolutions of $\varepsilon_{I_{mean}}$ and $\varepsilon_{I_{RMS}}$ with the number of images *N* for the 30° ramp case at Re_1 and Re_2 are shown in figure 2. The largest ramp is chosen because the induced SWBLI produces strong turbulence over the ramp surface, which normally requires a larger ensemble to achieve convergence. According to figure 2, $\varepsilon_{I_{mean}}$converges to a smaller magnitude than $\varepsilon_{I_{rms}}$, while $\varepsilon_{I_{mean}}$ also has narrower scattering.

Despite the differences, residuals for both I_{mean} and I_{RMS} are close to 0.01 counts when the full range of images are used, which corresponds to about 0.5% of the RMS schlieren intensity in the freestream region. For the purpose of clarity, the convergence curves for the other SWBLI cases are not shown, but they have similar features and their final residuals are also close to 0.01 count. Convergence can therefore be concluded for I_{mean} and I_{RMS}.

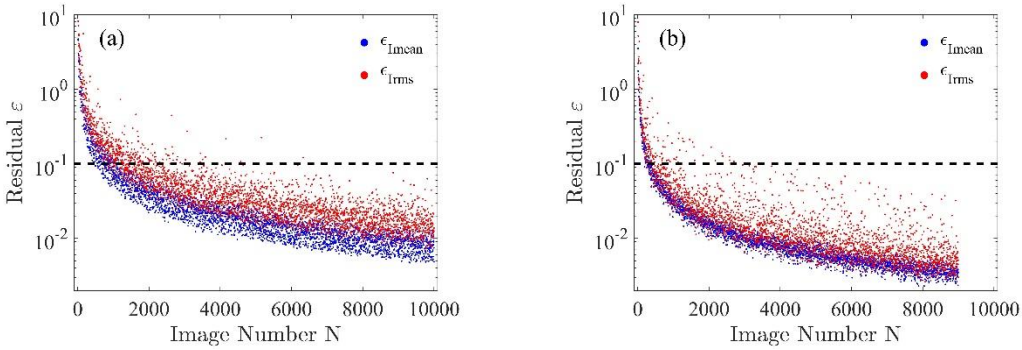

Fig. 2 The evolution of I_{mean} and I_{RMS} with the number of images N for the 30° ramp SWBLIs at Re_1 (a) and Re_2 (b).

III. Results and Analysis

A. Effect of Ramp Angle

The ramp angle effect is first explored through the SWBLIs at Re_1. The schlieren snapshots for the 6 compression ramps are shown together in figure 3. It is clear that increasing the ramp angle α gradually moves the separation shock wave upstream. The inviscid shock origination point is at $x/h = -0.6$ in the α=20° SWBLI, and it moves to $x/h = -1.5$ in the α=30° SWBLI, corresponding to a longer interaction zone. Verma *et al.* [15] reported an experiment on a 24° compression ramp SWBLI at Ma = 2.05, where the incoming boundary layer thickness is 3.85 mm. The interaction length of the SWBLI in [15] was about 20 mm, which is similar to its counterpart in figure 3(c). The reattachment shock wave gradually builds up strength following the increase of α. However, it is not as focused as the separation shock wave even in the 30° ramp SWBLI. The turbulent region over the ramp surface also becomes thicker over a steeper ramp. Its thickness is 0.2h over the 20° ramp and is thickened to nearly 0.5h over the 30° ramp. The separation shock waves in all the SWBLIs in figure 3 have a similar angle of 47°, suggesting that the flow deflection angle due to the ramp is alleviated by the turbulent wedge formed in the interaction zone. The reattachment shock wave can be clearly seen when $\alpha \geq 24°$, and it gets stronger over a larger compression ramp. Due to the upstream movement of the separation shock wave, the two shock waves are further separated following the increase of α.

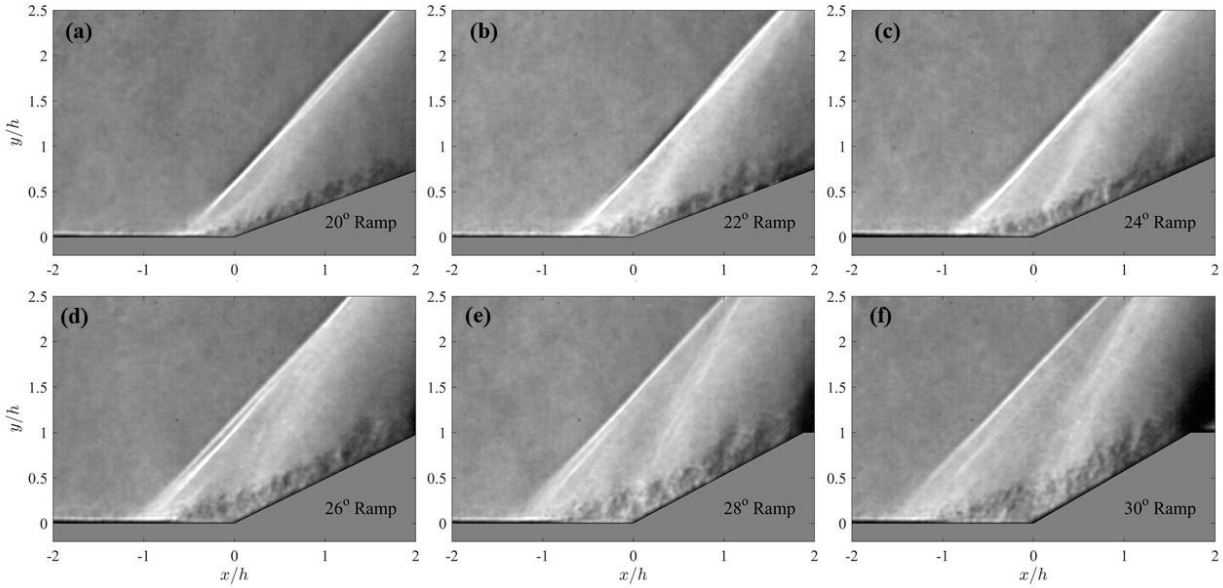

Fig. 3 Schlieren snapshots for SWBLIs at Re_1.

The short camera exposure time allows visualization of some transient flow features. The alternating bright and dark patterns can be observed in the interaction region and over the ramp, indicating the vortical activity. It will be revealed that all these moving structures contribute to the contoured distribution of the RMS schlieren intensity (I_{RMS}).

The I_{RMS} in the SWBLIs at Re_1 were calculated and are shown in figure 4. The I_{RMS} contour range is set from 1 to 12 counts, which is chosen to resolve the I_{RMS} distribution in the near wall turbulent region. Because the I_{RMS} associated with the shock wave is significantly stronger than the other part of the flow field, the shock waves in figure 4 are saturated by the red color. The separation shock wave remains strong for all the cases except its foot region close to the wall. This 'weak' foot region is usually comprised of compression waves and extends further above the wall for larger ramps. The reattachment shock wave is also represented by the concentration of I_{RMS}. It is clearly visualized in the SWBLIs when $\alpha = 28^o$ and 30^o, and it is only partially visualized near the triple point in the SWBLI when $\alpha = 26^o$.

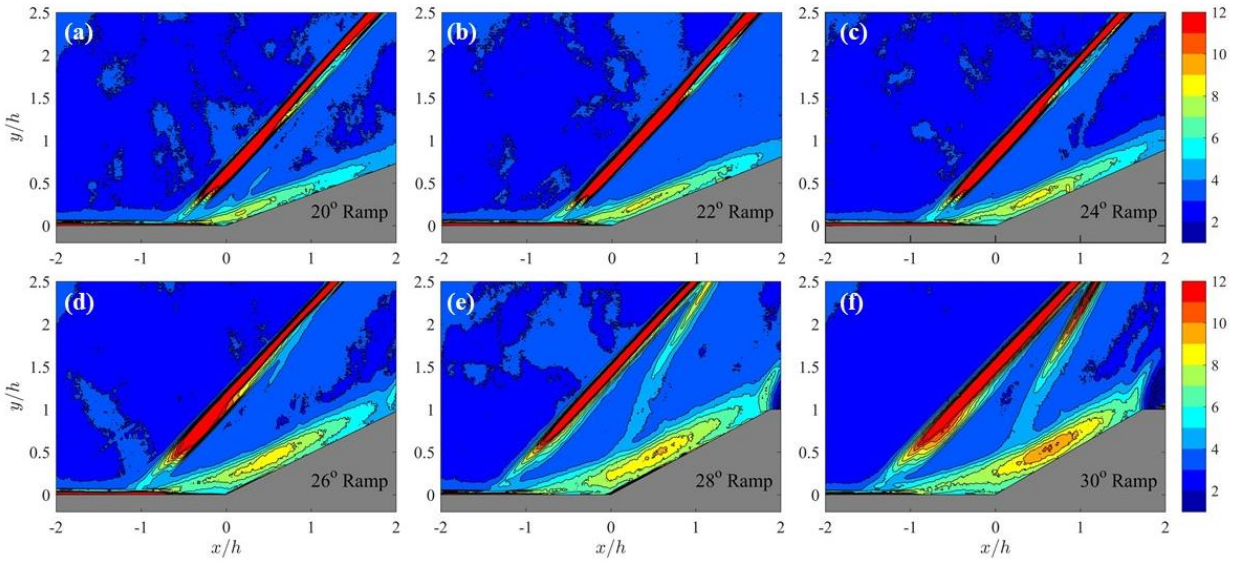

Fig. 4 Contours of I_{RMS} for SWBLIs at Re_1.

Due to the interaction of boundary layer and shock wave, the near wall region after the separation shock wave has much stronger I_{RMS} than that in the incoming turbulent boundary layer, which agrees with the observation in the raw schlieren snapshots in figure 3. Two sub-domains can be distinguished: one is the interaction zone and the other is the turbulent region over the ramp surface. The I_{RMS} in the latter sub-domain features a concentric elliptical distribution, where the position of peak I_{RMS} corresponds to the location of peak fluctuation of density gradient, which is likely linked to the strongest vortical event in the shear layer. The peak I_{RMS} magnitude becomes larger and it moves downstream over a steeper ramp. In the LES simulation of a SWBLI at a 25° compression ramp [12], a peak u_{RMS} is revealed over the ramp surface, and an increased level of velocity fluctuation happens along the separated shear layer. Although, the RMS of density variation was not presented in that work, as velocity and density fluctuations are closely correlated in compressible flow, enhanced density fluctuations can be conjectured in the separated shear layer and the turbulent region over the ramp.

Closer inspection on the I_{RMS} contours can detect a small region at the ramp corner, in which the I_{RMS} intensity is distinctively weaker than the surrounding area. Close-up views on this region are provided in figure **5**. This region of weak I_{RMS} is speculated to be in association with the separation bubble, which has less fluctuations than the separated shear layer. In the LES study mentioned earlier [12], the region of separation bubble was also found of weaker velocity

fluctuations than the separated shear layer. However, the relation between the low I_{RMS} region at the corner and the separation bubble still needs validation.

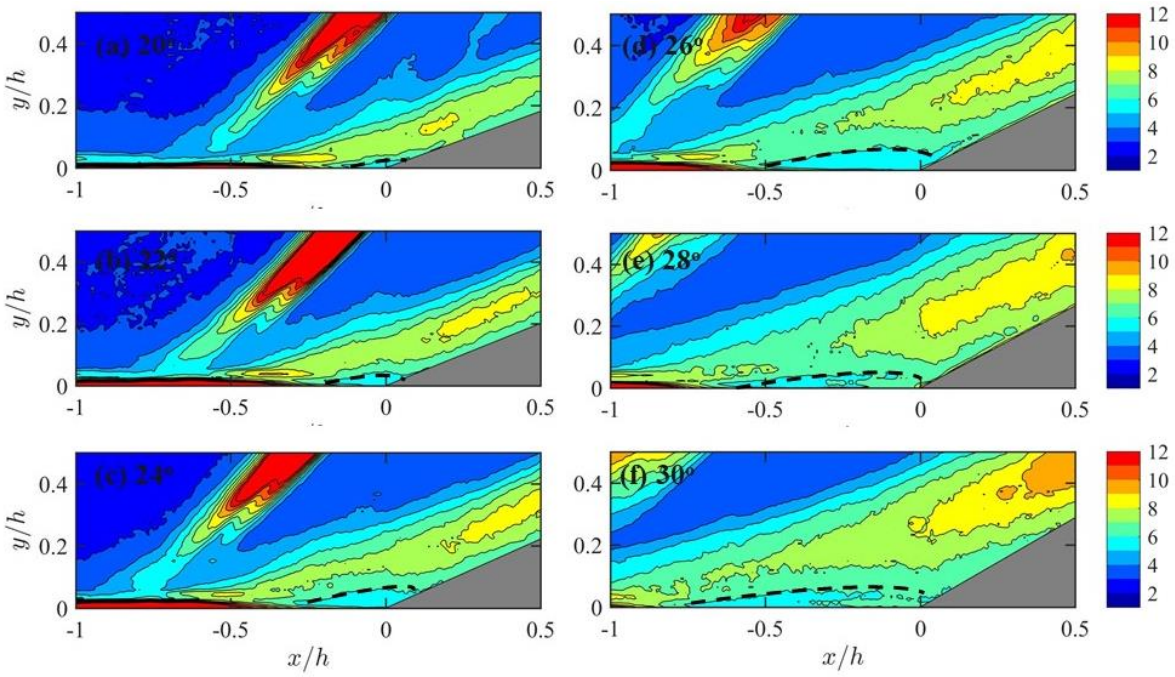

Fig. 5 Close-up view on the I_{RMS} contour at the ramp corner at Re_1. The dashed lines indicate the boundary of weak I_{RMS} region at the ramp corner.

B. Effect of Reynolds Number

In order to explore the Reynolds number effect, the SWBLIs at Re_2 are examined here. The schlieren snapshots for each case are shown in figure 6. The longer plate allows further development of the incoming turbulent boundary layer, resulting in a larger thickness of 4.4 mm at the location of the ramp. The present Reynolds number based on boundary layer thickness is Re_2=35,600. It should be mentioned that the schlieren images in figure 6 are slightly brighter than those in figure 3, despite the schlieren setup remaining unmoved in the experimental campaign. Since the measurements for Re_1 and Re_2 were performed in two consecutive days, the thermal effect and vibration might cause the slight displacement of cut-off knife.

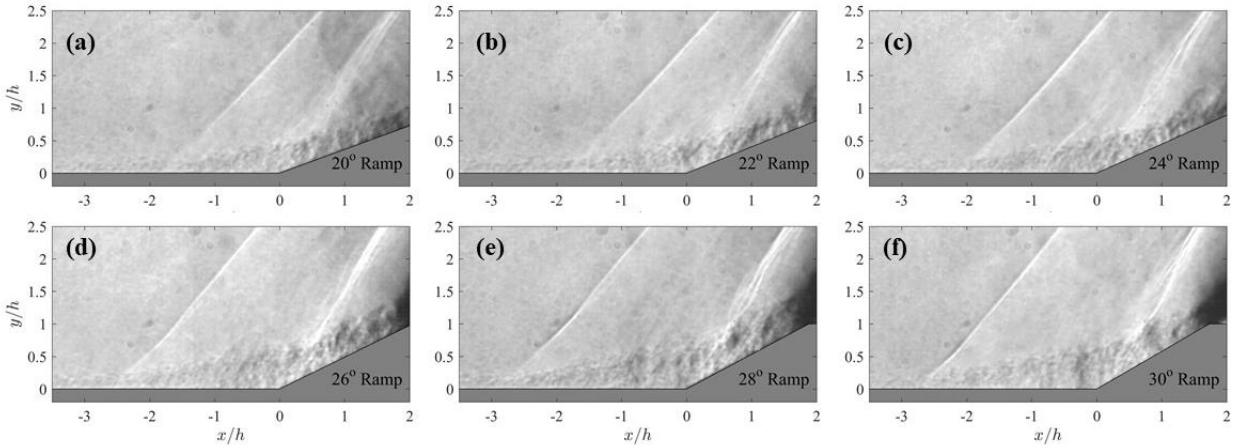

Fig. 6 Schlieren snapshots for SWBLIs at Re_2.

Comparing the SWBLIs at Re_1 and Re_2, it can be appreciated that the Reynolds number (or the boundary layer thickness) underpins the shock wave structure. The separation shock wave in the 20° ramp SWBLI has the inviscid origin at $x = -2h$, resulting in a much longer interaction region than that at Re_1. Increasing the ramp angle lengthens the interaction region. The growth of L_i with the ramp angle at both Reynolds numbers is shown in figure 7. Figure 7(a) reveals the growth of L_i/h. For the whole range of ramp angles, the L_i at Re_2 is about $1.2h$ longer than that at Re_1. A similar trend of L_i growth is resulted at both Reynolds numbers: the steepest increase happens when α =24° - 26°. However, if the boundary layer thickness δ is used for non-dimensionalization, the difference of L_i/δ is about 3 between the 20° ramp SWBLIs at Re_1 and Re_2, but it shrinks for steeper ramps. It should be pointed out that the L_i/δ at Re_1 and Re_2 are very close at the 28° and 30° ramps, suggesting that the boundary layer thickness could be a more appropriate scaling parameter for the interaction length when the ramp angle is larger than the largest flow deflection angle according to the inviscid oblique shock relation.

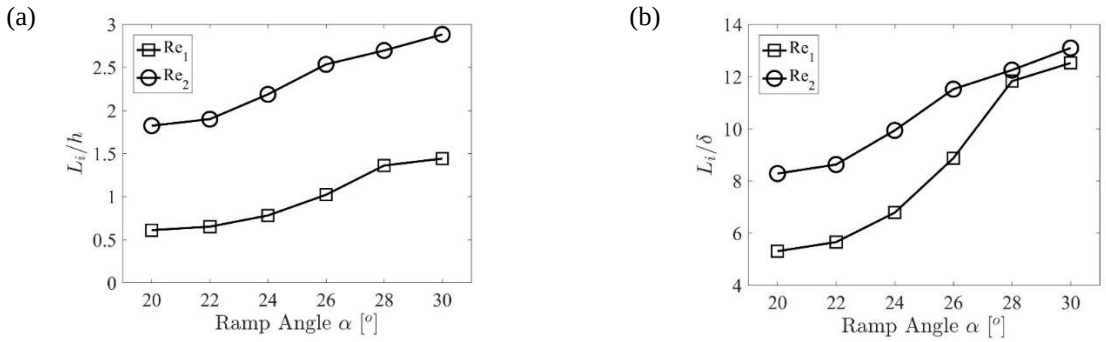

Fig. 7 Growth of interaction length L_i with ramp angle α at Re_1 and Re_2: (a) L_i scaled by h; (b) L_i scaled by δ.

Different from the Re_1 cases, the reattachment shock wave at Re_2 is visible in all the ramps. Moreover, the separation shock and reattachment shock do not coalesce in the present field of view. In another experimental visualization on the SWBLI at a 28° compression ramp at Ma=3.0 and Re_δ = 76,500 [16], a similar shock wave pattern was visualized, where separation and reattachment shock waves did not merge. The above discussion proves that the boundary layer thickness δ is an underpinning parameter for the shock wave structure.

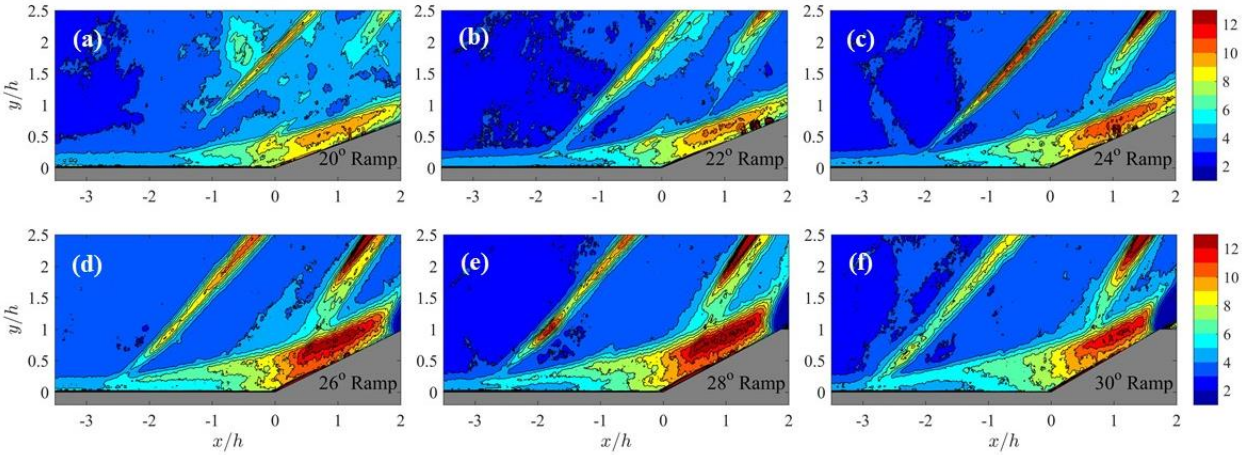

Fig. 8 Contours of I_{RMS} for SWBLIs at Re_2.

The contour of I_{RMS} for SWBLIs at Re_2 are shown in figure 8. The SWBLIs at Re_2, in general, result in stronger I_{RMS} magnitude over the ramp than their counterparts at Re_1. The separation and reattachment shock waves are represented by the high concentration of I_{RMS} in each SWBLI at Re_2. In contrast, the reattachment shock wave has much weaker I_{RMS} intensity at Re_1. Moreover, the thickness of both the interaction region and the turbulent region over the ramp at Re_2 are also significantly larger. The peak I_{RMS} for the 20° ramp at Re_2 is more than 10 counts. It seems the increase of peak I_{RMS} is not monotonic. The I_{RMS} over the 28° ramp has a peak magnitude over 13 counts, while that of the 30° ramp decreases slightly to 12 counts. The location of peak I_{RMS} moves downstream along the ramp from x/h=0.1 to 0.6 at Re_1. Differently, it does not exhibit large streamwise movement at Re_2.

The corner region of lower I_{RMS} magnitude observed in SWBLIs at Re_1 was conjectured in association with the separation bubble. A similar region of weaker I_{RMS} can be identified in SWBLIs when α=28° and 30° in figure 8. Instead of appearing right at the ramp corner, it is located between x/h = −2.5 ~ −1.4 for the 28° ramp and between x/h = −2.5 ~ −1.2 for the 30° ramp. But in the SWBLIs at the other smaller ramps, this region of weaker I_{RMS} does not

show up as a closed region and is open at its leading edge. It becomes partially closed in the 26° ramp. This gradual change of the low I_{RMS} region probably suggests the formation of the shock induced flow separation with the increase of ramp angle, but further evidence through velocity measurement is needed.

So far, the flow organization and the fluctuation in the SWBLIs at six ramp angles and two different Reynolds numbers have been discussed. In the next section, the unsteady motion of the shock waves will be analyzed through spectral analysis.

C. Shock Wave Unsteadiness

The schlieren images are used as an optical sensor to study the shock wave oscillation. A shock wave detection algorithm is developed, where the shock wave position is identified through the maximum gradient of the schlieren intensity across the streamwise direction. Since the entire ensemble is used, the resulted temporal sequence of shock wave position contains 10,000 points and 9,000 points for Re_1 and Re_2 cases, respectively. In an earlier experimental study on the unsteady shock wave induced by a vertical cylinder [17], the shock wave was detected in the high-speed schlieren images recorded at 100 kHz, and the shock wave motion was verified by pressure sensors. This imaged-based technique was further employed to study the shock wave unsteadiness in a transitional boundary layer and shock wave interaction [18]. In the present study, the shock waves at the height of y/h=1.5 are investigated, as the separation and reattachment shock waves are strong and clear at this height in both Reynolds number cases. The standard Fast Fourier Transformation (FFT) is applied to retrieve the spectrum of the shock wave unsteadiness. Since 2^{13} points are used in the FFT operation, the resulted frequency resolution is 2.44 Hz.

The pre-multiplied spectra $f \cdot P(f)$ of the separation shock in SWBLIs at Re_1 are organized into a contour plot in figure 9, so that spectral variation in relation to ramp angle can be studied. Increased spectral intensity can be observed in the frequency band of 100-1,000 Hz, and it centers at about 600 Hz (St_δ = 0.0026), which agrees with the established knowledge of low-frequency unsteadiness. The peak spectral intensity for the low-frequency unsteadiness becomes stronger under a larger ramp angle. It should be mentioned that the narrow peak at 22 Hz in all the ramps is associated with the model vibration, which is due to the model's vertical cantilever type installation.

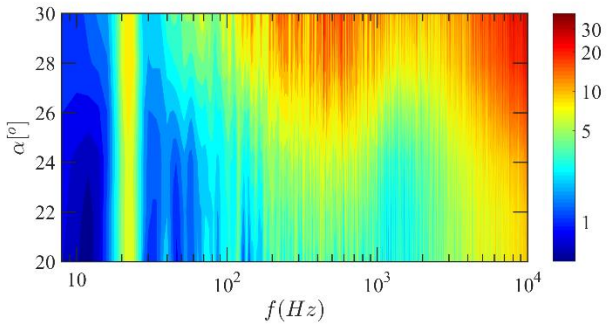

Fig. 9 Pre-multiplied spectra $f \cdot P(f)$ [unit: mm/s] of the separation shock wave oscillations at *y/h*=1.5 in SWBLIs at Re_1.

The reattachment shock can be faithfully detected only when the ramp angle is larger than 28° at Re_1. The pre-multiplied spectrum of the reattachment shock for the 28° ramp is shown in figure 10(a) as an example, where that of the separation shock is also included for comparison. It should be noted that the spectra shown in figure 10 and figure 12 are processed through the Welch method using blocks of 512 samples and the Hamming window function with 50% overlap. This operation is employed to filter out the random noise in the original spectra shown in figure 9 and figure 11, but at the expense of a reduced frequency resolution, namely a frequency resolution of 39 Hz. According to figure 10(a), the reattachment shock wave also exhibits intensified magnitude in the low-frequency band. The peak magnitude of the reattachment shock happens at 820 Hz (St_δ = 0.0037), which is slightly larger than that of the separation shock, whose peak is at 660 Hz (St_δ = 0.0030). Sartor et al. [19] studied the unsteady shock wave in a transonic SWBLI on a baseline shock generation bump. It revealed that the reattachment shock wave motion is closely correlated with the vortical activity in the separated shear layer, where the reattachment shock originates. Similarly, the reattachment shock frequency in the present SWBLI should also indicate the characteristic frequency of the vortex shedding activity in the separated shear layer over the compression ramp.

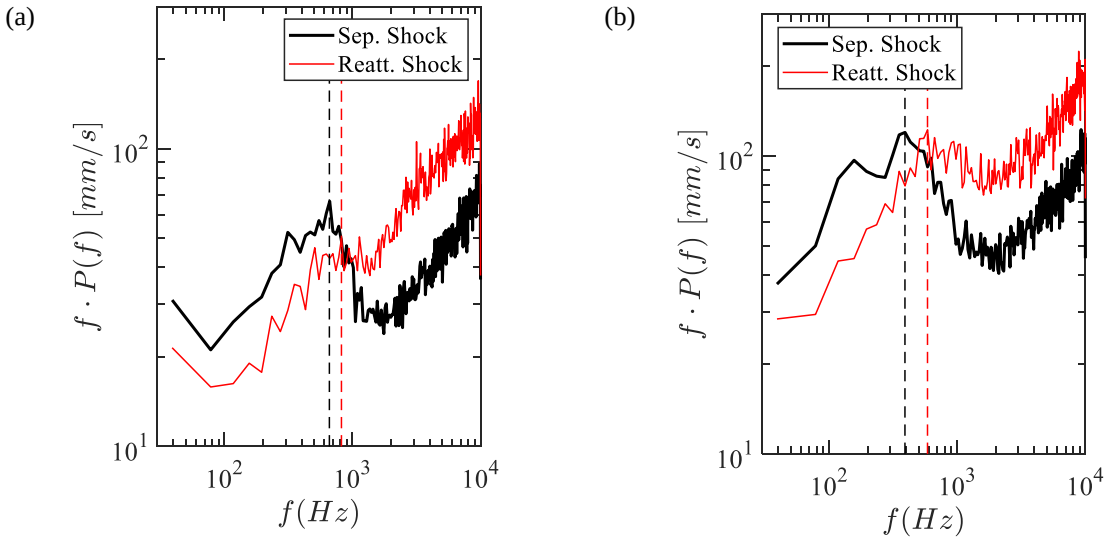

Fig. 10 Pre-multiplied spectra of the separation and reattachment shock waves in the 28° ramp SWBLIs at Re_1 (a) and Re_2 (b). The vertical dashed lines are the central frequency of the low-frequency unsteadiness of both shock waves.

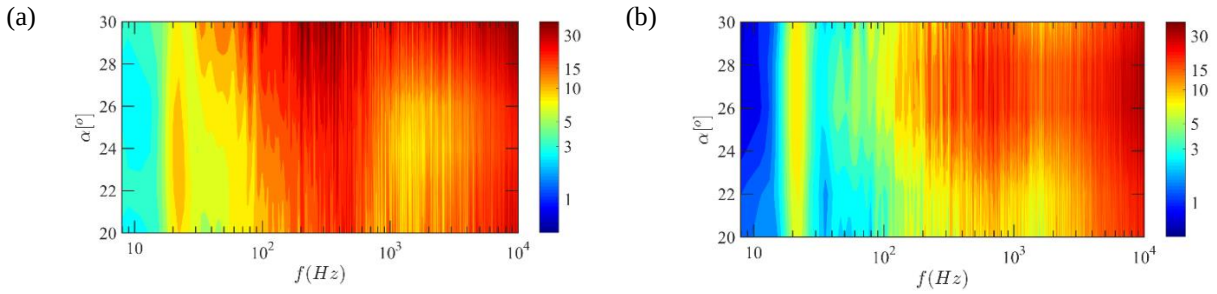

Fig. 11 Pre-multiplied spectra $f \cdot P(f)$ [unit: mm/s] of the separation (a) and reattachment (b) shock wave oscillations at *y/h*=1.5 in SWBLIs at Re_2.

The pre-multiplied spectral contours for both shock waves at Re_2 are shown in figure 11. Not surprisingly, the contour of separation shock spectra has the low-frequency unsteadiness, whose intensity also increases with the ramp angle. However, the peak of present low-frequency unsteadiness appears at around 400 Hz, which is smaller than that at Re_1. In order to better appreciate the Reynolds number effect on the shock wave unsteadiness, the separation shock spectra in the 28° ramp SWBLIs at both Reynolds numbers are compared in figure 12(a). Despite the broadband feature across the low-frequency domain, the separation shock spectrum at Re_2 exhibits stronger

magnitudes, while its peak frequency shifts towards a lower frequency around 390 Hz, which is smaller than that of the separation shock at Re_1.

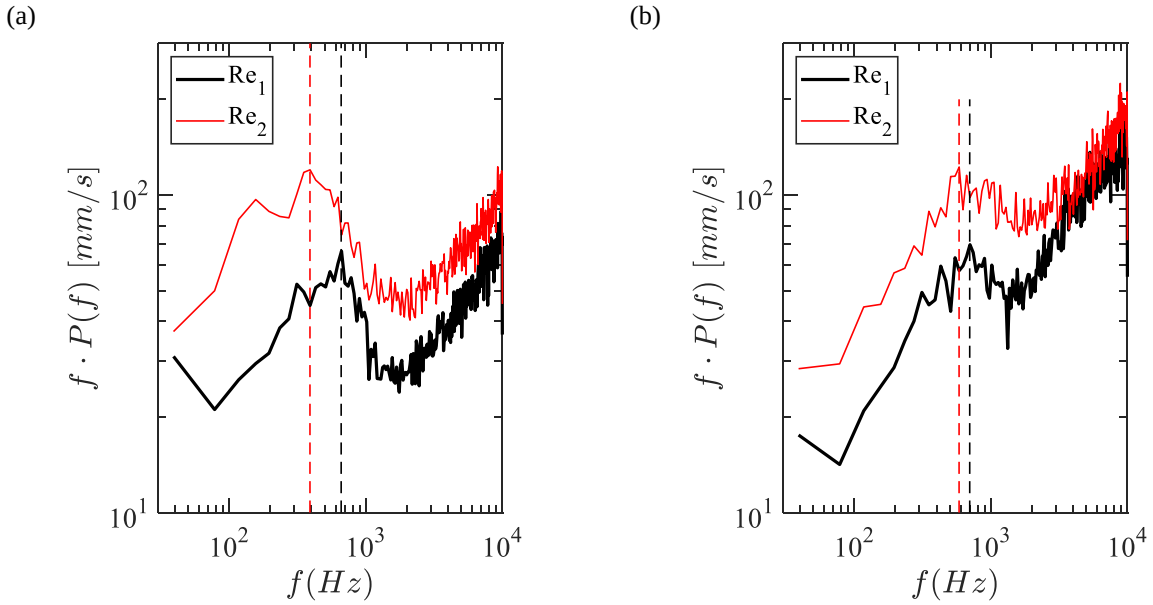

Fig. 12 Pre-multiplied spectra $f \cdot P(f)$ [unit: mm/s] of the separation (a) and reattachment (b) shock wave oscillations at y/h=1.5 in the 28° ramp SWBLIs at Re_1 and Re_2.

The spectral contour of the reattachment shock at Re_2 is shown in figure 11(b). Similar as the separation shock, the reattachment shock's intensity of low-frequency unsteadiness increases with ramp angle. However, it seems that a slight decrease in intensity happens in the 30° ramp spectrum. A closer comparison between the two spectral contours in figure 11 reveals that the peak frequency for both shock waves at Re_2 becomes smaller than that at Re_1. This observation is further supported by the shock wave spectra in the 28° ramp SWBLI at Re_2, see figure 10(b). The peak frequency of the separation shock and reattachment shock reduces to 390 Hz and 585 Hz respectively, which are smaller than their counterparts at Re_1.

The Reynolds number effect on the reattachment shock is finally explored through the shock wave spectra over the 28° ramp, see figure 12(b). As revealed earlier, although the peak frequency shifted from 820 Hz to 585Hz when Reynolds number increased from Re_1 to Re_2, this change in peak frequency is less than that of the separation shock. Hence, Reynolds number effect on spectrum modulation is weaker for the reattachment shock wave.

IV. Conclusions

Through the present experimental investigation on SWBLIs at compression ramps, the high-speed schlieren has been demonstrated as a powerful tool in examining the resulted flow organization and unsteadiness. The converged RMS schlieren intensity I_{RMS} enables visualization of flow structures that are not immediately available in the raw schlieren snapshot, such as the peak turbulent region over the ramp surface, and the region of weaker I_{rms} at the ramp corner. The latter was conjectured as a representation of the separation bubble, but further validation is needed.

The effects of ramp angle and Reynolds number on the compression ramp SWBLI have been examined. The interaction strength was varied by using ramps with angle between 20^o and 30^o. The interaction length grew with the ramp angle, while the steepest increase took place in the 24^o and 26^o ramps. Moreover, a steeper ramp resulted in a stronger interaction, namely a thicker turbulent region and a stronger I_{RMS} magnitude. The Reynolds number was changed by increasing the thickness of the incoming turbulent boundary layer. The structure of the SWBLI was altered significantly by increasing the Reynolds number. The interaction region became longer and the turbulent region over the ramp surface was stronger. Most of all, the reattachment shock appeared in all the SWBLIs at Re_2, whereas it could only be clearly observed over the 28^o and 30^o ramps at Re_1.

The shock wave unsteadiness was examined in the end. The typical low-frequency oscillation was clearly revealed in the shock wave spectra. A larger ramp angle gave rise to a stronger spectral intensity in the low-frequency band. The Reynolds number or the thickness of turbulent boundary layer affected the shock wave's unsteadiness. The SWBLI under the same ramp Re_2 obtained stronger spectral intensity in the low-frequency band. Moreover, Reynolds number was effective in frequency modulation. The larger Reynolds number resulted in a lower peak frequency for both separation and reattachment shock waves. In the present experiment, the reduction in peak frequency is 270 Hz and 235 Hz for the separation shock and reattachment shock, respectively.

The present experimental work using high-speed schlieren with short exposure time provides fundamental understanding of the compression ramp SWBLIs and paves the foundation for future experiments using other quantitative measurement techniques, such as particle image velocimetry, through which some of the observations and the associated conjectures can be further quantified and confirmed.

Acknowledgement

This research is supported by UK Royal Society (RSG\R1\180236), UK Engineering Physical Sciences Research Council (EP/R013608/1), and Natural Science Foundation of China (51522606, 11902360).

References

[1] Dolling, D.S. "Fifty Years of Shock-Wave/Boundary-Layer Interaction Research: What Next?", AIAA J (2001) 39(8):1517.

[2] Priebe, S. & Pino Martin, M., Low-frequency unsteadiness in shock wave-turbulent boundary layer interaction, J. Fluid Mech. (2012) 699: 1.

[3] Pasquarieilo, V., Hickel, S., Adams, N.A., Unsteady effects of strong shock-wave/boundary-layer interaction at high Reynolds number, J. Fluid Mech. (2017) 823: 617.

[4] Gaitonde, D.V., Progress in shock wave/boundary layer interactions, Prog. Aero. Sci. (2015) 72:80.

[5] Chang, J., Li, N., Xu, K., Bao, W. & Xu, D., Recent research progress on unstart mechanism, detection and control of hypersonic inlet, Prog. Aero. Sci. (2017) 89:1.

[6] Babinsky, H. & Harvey, J.K., Shock wave-boundary-layer interactions, Cambridge University Press (2012) 1st ed.

[7] Zheltovodov A.A., Shock waves/turbulent boundary-layer interactions – fundamental studies and applications, AIAA Paper 1996-1977.

[8] Loginov M.S., Adams N.A. & Zheltovodov A.A., Large-eddy simulation of shock-wave/turbulent-boundary-layer interaction, J. Fluid Mech. (2006) 565:135.

[9] Muzio G., Peter, F., Hickel, S. & Adams, N.A, Large-eddy simulation of a supersonic turbulent boundary layer over a compression-expansion ramp, Int. J. Heat & Fluid Flow (2013) 42:79.

[10] Dupont, P., Haddad, C. & Debieve, J.F., Space and time organization in a shock-induced separated boundary layer, J. Fluid Mech. (2006) 559: 255.

[11] Clemens, N.T., Narayanaswamy, V., Low-frequency unsteadiness of shock wave/turbulent boundary layer interactions, Annu. Rev. Fluid Mech. (2014) 46:469.

[12] Grilli, M., Schmid P.J., Hickel, S. & Adams, N.A., Analysis of unsteady behaviour in shockwave turbulent boundary layer interaction, J. Fluid Mech. (2012) 700: 16.

[13] Laurence, S.J., Wagner, A. & Hannemann, K., Schlieren-based techniques for investigating instability development and transition in a hypersonic boundary layer, Exp Fluids (2014) 55: 1782.

[14] Combs, C.S., Schmisseur, J.D., Bathel, B.F., & Jones, S.B., Unsteady analysis of shock-wave/boundary-layer interaction experiments at Mach 4.2. AIAA Journal, 1–10. doi:10.2514/1.j058073

[15] Verma, S.B., Manisankar, C. & Raju, C., Control of shock unsteadiness in shock boundary-layer interaction on a compression corner using mechanical vortex generators, Shock Waves (2012) 22:327-339.

[16] Wu, Y., Yi, S., He, L. & Chen, Z., Flow visualization of Mach 3 compression ramp with different upstream boundary layers, J. Vis. (2015) 18: 631.

[17] Combs, C.S., Kreth, P.A., Schmisseur, J.D. & Lara Lash E., Image-based analysis of shock-wave/boundary layer interaction unsteadiness, AIAA J. (2018) 56:1288.

[18] Combs, C.S., Lara Lash, E., Kreth, P.A. & Schmisseur, J.D., Investigating unsteady dynamics of cylinder-induced shock-wave/transitional boundary-layer interactions, AIAA J. (2018) 56: 1588.

[19] Sartor F., Mettot C., Bur R. & Sipp D., Unsteadiness in transonic shock-wave/boundary layer interactions: experimental investigations and global stability analysis, J Fluid Mech. (2015) 781:550-577.